Sustainable Food Technology

PAPER

View Article Online
View Journal | View Issue

Cite this: *Sustainable Food Technol.*, 2024, **2**, 447

Biogenic-magnesium oxide nanoparticles from *Bauhinia variegata* (Kachnar) flower extract: a sustainable electrochemical approach for vitamin-B_{12} determination in real fruit juice and milk†

Sarita Shaktawat, Rahul Verma, Kshitij RB Singh and Jay Singh *

Vitamin-B_{12} (Vit-B_{12}) is an essential organo-metallic micronutrient necessary for the proper functioning of the human body. Factors such as convenient lifestyle, starvation, and genetic defects are major contributing reasons for Vit-B_{12} deficiencies, which can lead to increased morbidities. Today's challenge lies not only in advancing the diagnosis of Vit-B_{12} but also in making it sustainable. In this context, the electrochemical detection of Vit-B_{12} was performed utilizing hydrothermally synthesized biogenic-magnesium oxide nanoparticles (B-MgO-NPs) derived from Kachnar (Bauhinia variegata) flower extract. After the synthesis of B-MgO-NPs, XRD, FTIR, Raman, UV-vis, XPS, SEM, EDX, and HR-TEM techniques were used to determine their structural and morphological characteristics. Electrochemical analysis results suggest that the fabrication of electrophoretically deposited B-MgO NPs on an indium tin oxide (ITO) glass substrate-based bioelectrode has more current density when compared with bare ITO. Moreover, it was also evident from cyclic voltammetry analysis that the fabricated bioelectrode exhibited sensitivities of 2.96×10^{-3} and 0.17×10^{-3} mA pM^{-1} cm^{-2} in a linear concentration range of 1–100 and 200–1200 pM, respectively. Furthermore, it demonstrated a low limit of detection (LOD) of 0.0884 pM and a limit of quantification (LOQ) of 1.3462 pM. Apart from standard sample analysis, the B-MgO NP/ITO bioelectrode was used to quantify real samples, such as preservative juice, fresh milk, orange juice, and vitamin-B_{12} tablets. Thus, the fabricated bioelectrode is reliable for real sample analysis. This study is important in the field of Vit-B_{12} detection, aiding in quality control, product development, and nutritional assessments.

Received 21st October 2023
Accepted 1st February 2024

DOI: 10.1039/d3fb00198a

rsc.li/susfoodtech

Sustainability spotlight

The synthesis of B-MgO NPs (biogenic-magnesium oxide nanoparticles) through a green route using Kachnar flower extract is considered an eco-friendly and biocompatible approach. The utilization of natural extracts, such as Kachnar flower extract, in the synthesis process adds to the environmentally friendly nature of the method. These extracts can act as reducing agents or stabilizers, eliminating the need for harsh chemicals or energy-intensive processes typically associated with nanoparticle synthesis. The resulting B-MgO NP/ITO (indium tin oxide) bioelectrode is designed to be used as an electrochemical biosensor specifically for detecting vitamin B_{12} (Vit-B_{12}). The bioelectrode exhibits high sensitivity and selectivity towards Vit-B_{12}, making it capable of accurately detecting and quantifying this vitamin. One notable characteristic of the B-MgO NP/ITO bioelectrode is its ultralow limit of detection (LOD) of 0.088 pM (picomolar), making it possible to detect even extremely low concentrations of Vit-B_{12} with high precision. The detection range of 10–1200 pM further demonstrates the versatility and applicability of the biosensor in detecting a wide range of Vit-B_{12} concentrations. To evaluate the practical applicability of the electrochemical biosensor, it has been tested on real samples. This testing allows researchers to assess the biosensor's performance in real-world scenarios, ensuring its reliability and accuracy when used to detect Vit-B_{12} in actual samples. Overall, the use of B-MgO NPs synthesized *via* a green route with Kachnar flower extract, combined with the B-MgO NPs/ITO bioelectrode for Vit-B_{12} detection, demonstrates an eco-friendly and biocompatible approach to biosensor development. The high sensitivity, selectivity, and low limit of detection make it a promising tool for various applications in fields such as healthcare, food analysis, and environmental monitoring.

1. Introduction

Vitamin-B_{12} (Vit-B_{12}) is an essential cobalt metal-containing, water-soluble organometallic micronutrient called cyanocobalamin or cobalamin. Vit-B_{12} controls a myriad of human body

Department of Chemistry, Institute of Sciences, Banaras Hindu University, Varanasi 221005, Utter Pradesh, India. E-mail: jaysingh.chem@bhu.ac.in; Tel: +91 9871766453

† Electronic supplementary information (ESI) available. See DOI: https://doi.org/10.1039/d3fb00198a

Table 1 Several analytical methods, such as HPLC, immunoassays, and microbiological detection, essential for determining vitamin B_{12} concentration in foods, medicines, and biological materials

S. no.	Name of technique	Platform for detection	Some other important points	Lower limit of detection (LOD)	Time consumption and cost	Drawbacks	Ref.
1	Microbiological detection	Microorganisms (*Lactobacillus leishmania*)	Culture microorganism, 24 h in skim milk-based medium (first technique for detection of Vit-B_{12})	20 pg mL^{-1}	Time consuming process/costly	Blood serum effect contains additional factors like antibiotics; these prevent growth of the microorganism	7 and 8
2	Immunoassays	Enzyme-linked immunosorbent assays (ELISAs)	Immobilized rabbit antibodies that capture cobalamin	2.2 pg mL^{-1}	Time consuming process/costly	Long and numerous steps in the process of preparing antibody plates	9 and 10
3	High-performance liquid chromatography (HPLC)	Microporous column	Liquid mixture of sample passing through a microporous column (first isolation technique of Vit-B_{12})	80 ng mL^{-1}	Time consuming/costly	Identifying Vit-B_{12} in prefab samples, such as food and dietary supplements	11 and 12
4	Capillary electrophoresis (CE)	Electro-osmosis	Liquid electrolyte and high voltage (15 kV)	20 μg mL^{-1}	25 min and costly	Separation of different cobalamin *via* capillary action	13
5	Radioisotope and mass spectrometry	Radioactive isotope ^{57}Co and ^{14}C	The radioactive blood plasma; MS ionizes the sample	100 fg mL^{-1}	Time consuming/costly	Complicated, costly, and complex experimental setup	14 and 15
6	Optical detection techniques (ODT)	Light interaction with sample	Trustable and sensitive technique for the detection of biomolecules like DNA, protein, and vitamins (ODT for the detection of Vit-B_{12} fluorescence detection, Raman scattering)	250 ng mL^{-1}	Time consuming/costly	Expensive, complicated handling process	16
7	Chemiluminescence (CL)	Lab-on-a-chip method	Interaction of vitamins with light-emitting molecules, like luminal	9.3 ng mL^{-1}	Faster/costly	Cross-sensitivity to other metal ions	17–19
8	Adsorption and fluorescence	Intrinsic absorption or other light emitting species	Interaction between Vit-B_{12} and fluorescence	2 μg mL^{-1}	Faster/costly		20 and 21
9	Surface plasmon spectroscopy (SPR)	Oscillation of electrons along the metal and dielectric surface interfaces	Oscillation process is sensitive towards the refractive index of the environment	1 μg mL^{-1}	Faster/costly	Depends on the refractive index of the sample medium	22 and 23

functions, such as cell growth, energy production, neurological function, production of RBCs, DNA synthesis, myelination, and the cardiovascular system.[1] Vit-B_{12} is converted into two biological metabolically active forms, methyl cobalamin and 5-deoxyadenosylcobalamin.[2] The level of Vit-B_{12} in healthy human serum is between 200 pM and 900 pM.[3] The source of Vit-B_{12} is meat, eggs, liver, fish, clams, milk, vegetables, and fruits. Approximately 1–2 μg of Vit-B_{12} is necessary for the human body to sustain metabolic and physical activities, such as growth, age, and libido.[4] Breathing difficulty, tiredness, and atrophic gastritis are the common symptoms of Vit-B_{12} deficiency in the human body.[5] Severe Vit-B_{12} deficiency can result in serious disorders, such as megaloblastic and pernicious anemia, neurological disorders, and immunological disorders.[6] The development of techniques to measure vitamin B_{12} levels is critical because of the global problem of a lack of sophisticated methods for the detection of vitamin B_{12}. Table 1 lists and briefly describes several analytical methods that are essential for determining Vit-B_{12} concentration in foods, medicines, and biological samples.

However, these techniques are complicated, time-consuming, costly, and hazardous. The current challenge is to develop approaches that are not only sensitive and selective but also eco-friendly for the quantification of Vit-B_{12}.[1] Electrochemical analysis is a sensitive, selective, cost-effective, and convenient technique for the detection of Vit-B_{12}.[24]

Nanomaterials have a large surface area and conducting and electromagnetic properties,[25] which can be utilized to achieve safe and eco-friendly and sustainable protocols.[26] Thomele *et al.* reported that metal oxide nanoparticles have shown transformational behavior in aqueous environments. The metal oxide nanoparticles were characterized by various interaction pathways, such as dissolution–recrystallization and oriented attachment processes.[27] Heavy metals are characterized by their inherent toxicity, risks, as well as their nano-metabolizable nature and possible accumulation in the food chain.[28] Bozdogan *et al.* fabricated a Vit-B_{12} biosensor using synthesized peptide nanotubes from a disposable pencil graphite electrode system.[29] The detection of Vit-B_{12} and Vit-C has been performed in real samples through a miniaturized laser-induced graphene platform. This graphene-based bipolar platform study of Vit-B_{12} and Vit-C was achieved through an electrochemiluminescence technique.[30] Rajeev *et al.* fabricated a Ag-PEDOT/PGE (Silver-poly(3,4-ethylenedioxythiophene)/pencil graphite electrode) for the facile and economic electrochemical detection of methylmalonic acid.[31] A PdAu-PPy tailored carbon fiber-based paper electrode was fabricated successfully to perform an electrochemical study of methylmalonic acid (MMA) as a biomarker of Vit-B_{12} deficiency. The fabricated heavy metal-based PdAu-PPy electrochemical biosensor of MMA is facile, sensitive, and non-enzymatic, but it is hazardous and toxic.[24]

The biogenic magnesium oxide nanoparticle (B-MgO NPs) is an alternative to these Vit-B_{12} biosensors. B-MgO NPs is biocompatible, and an eco-friendly cubic crystal has been synthesized by green route *via* the Kachnar (*Bauhinia Variegata*) flower extract. The MgO is an interesting metal oxide having specific properties, such as biodegradability, ease of being metabolized, nontoxicity, surface catalytic properties, and chemical and thermal stability.[25] Several techniques are available for the synthesis of MgO NPs, such as direct transformation,[32] hydrothermal method,[33] microwave radiation,[34] vapor–solid process,[35] laser ablation,[36] sol–gel,[37] solid-state interfacial diffusion reaction[38] and others.[39] Kachnar is phytochemical-rich (alkaloids, terpenoids, flavonoids, amino acid and carbohydrates) medicinal plant that has been used as an anti-diabetic, anti-dyslipidemia and nephroprotective agent.[40] These phytochemicals are utilized as a capping, reducing, and stabilizing agent for the formation of B-MgO NPs. In summary, the synthesized B-MgO NPs exhibit eco-friendly, nontoxic, biodegradable, and biocompatible properties. Additionally, they demonstrate sensitivity and selectivity towards Vit-B_{12}, which has been detected using cyclic voltammetry (CV) and differential pulse voltammetry (DPV) with electrochemical detection. The detection of Vit-B_{12} was achieved by electrophoretically depositing B-MgO NPs onto an ITO (indium tin oxide) electrode. The resulting B-MgO NP/ITO bioelectrode was successfully utilized as a Vit-B_{12} biosensor, enabling the analysis of both standard and real solutions of Vit-B_{12}. The fabricated B-MgO NP/ITO bioelectrode material is suitable and highly effective in detecting Vit-B_{12}.

2. Experimental section

2.1. Materials and methods

Initially, 20 mL of a 0.1 M solution of magnesium nitrate hexahydrate (Merck, 99%) [$Mg(NO_3)_2 \cdot 6H_2O$] with a precursor weight of 512.82 mg was taken. To achieve a pH of 12, 5 M NaOH (Fisher Scientific) was added dropwise. Subsequently, 10 mL of Kachnar (*Bauhinia Variegata*) flower extract was slowly added, resulting in an immediate color change from milky white to dark green. The reaction mixture was then transferred to a Teflon container placed in a hydrothermal cell and left for 24 hours. The muffle furnace temperature was set to 180 °C. After thermal treatment, the sample was collected and centrifuged at 9500 rpm for 10 minutes. The resulting precipitate was washed with water, and this process was repeated two more times. The overall process of nucleation of B-MgO NPs, starting from the salt of magnesium to the formation of magnesium nanoparticles, is briefly described in eqn (1). The synthesized material was then dried under vacuum for further investigation. Fig. 1 shows a schematic representation of the synthesis process of B-MgO NPs, and its function in fabricating an electrochemical biosensor.

$$[Mg(NO_3)_2] \cdot 6H_2O + NaOH \rightarrow Mg(OH)_2 \rightarrow MgO \quad (1)$$

2.2. Preparation of the standard stock solution of vitamin-B_{12}

To prepare a 1 mM standard stock solution of vitamin B_{12} (Sigma), 1.35 mg of vitamin B_{12} was dissolved in 1 mL of double-distilled water. This standard stock solution was then used to facilitate the preparation of diluted solutions at 1 μM and 1 nM concentrations. For the preparation of a 1 μM standard stock solution, 1 μL of the 1 mM vitamin B_{12} stock solution was diluted in 1 mL of distilled water. Similarly, for the preparation

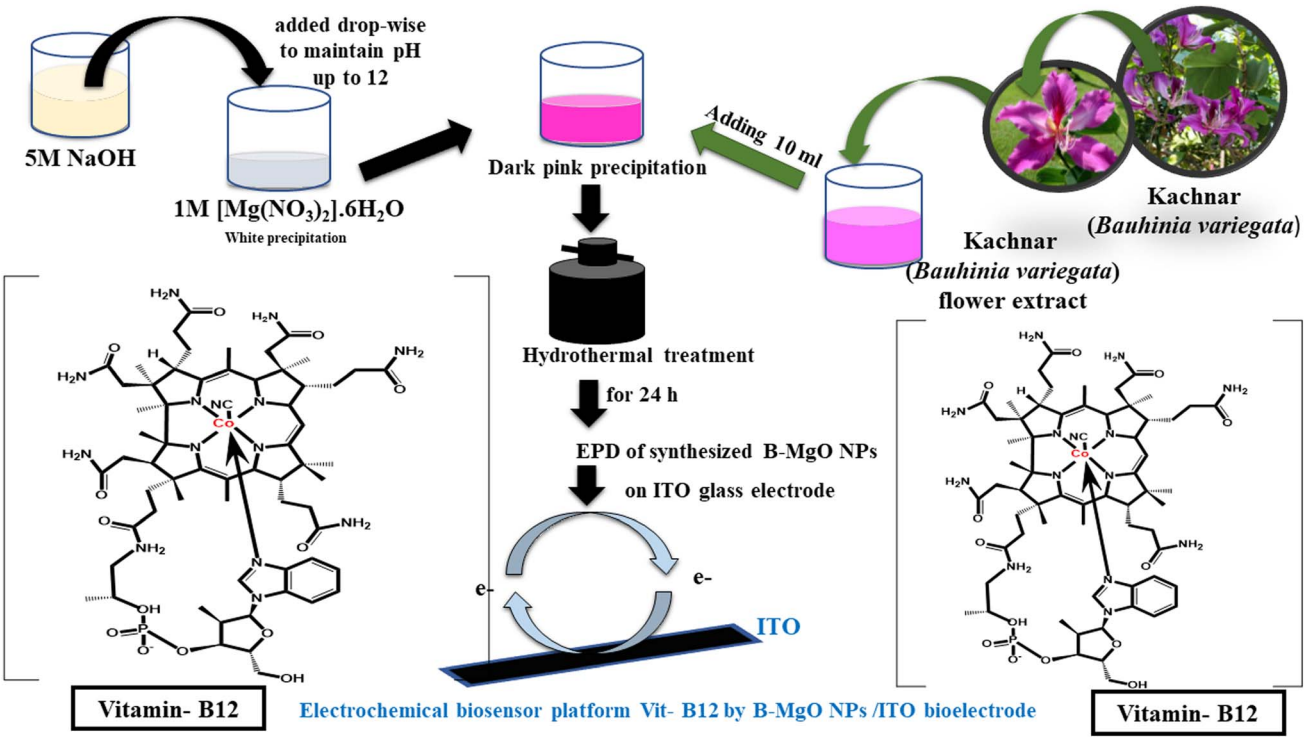

Fig. 1 Schematic presentations of the green route synthesis of the B-MgO NPs using the Kachnar (Bauhinia Variegata) flower extract, and the prepared electrochemical biosensor platform for Vit-B_{12}.

of a 1 nM standard stock solution, 1 μL of the 1 μM vitamin B_{12} stock solutions was diluted in 5 mL of distilled water. The prepared 1 nM standard stock solution was further diluted within the concentration range of 10 pM to 1200 pM for subsequent investigations. This range of diluted solutions was used to analyse the detection of vitamin B_{12} on the B-MgO NP/ITO bioelectrode.

2.3. Fabrication of the B-MgO NP/ITO electrode

To detect Vit-B_{12}, electrophoretic deposition (EPD) of B-MgO NPs on a conducting supporting surface of ITO glass electrode was performed using an electrophoresis unit (Genetix-GX300C). A physical binding of B-MgO NPs to the conducting surface of the ITO glass electrode was achieved through EPD. For EPD, a uniform colloidal solution of 15 mL was prepared by mixing an 80 : 20 ratio of de-ionized water and ethanol with 1 g of B-MgO NPs. The dispersion of B-MgO NPs was achieved by sonicating the EPD solution for 1 hour. A copper rod and hydrolyzed ITO glass electrode were used as the anode and cathode, respectively. These electrodes were placed parallel to each other, separated by approximately 1 cm, and immersed in the colloidal solution of B-MgO NPs. EPD is an excellent technique for the thin and even distribution of B-MgO NPs on the ITO glass surface (0.25 cm^2). Using the electrophoresis unit, the colloidal solution of B-MgO NPs was drop-casted onto the ITO glass at a maintained potential of 0.50 mV for 5 seconds. The fabricated modified B-MgO NP/ITO bioelectrode was used for the electrochemical sensing of Vit-B_{12}.

2.4. Mechanistic pathway for the electrochemical determination of Vit-B_{12}

A phosphate buffer with a pH of 7.5 was used in the electrochemical detection of Vit-B_{12} using a three-electrode cell system on a B-MgO NP/ITO electrode with a surface area of 0.25 cm^2. The PBS contained $K_4[Fe(CN)_6]$ and $K_3[Fe(CN)_6]$ as mediator ions between the B-MgO NP/ITO bioelectrode and Vit-B_{12}. The electrochemical study of the B-MgO NP/ITO bioelectrode was conducted using a three-electrode cell system. The working electrode consisted of a 0.25 cm^2 area of the B-MgO NP/ITO bioelectrode dipped in a phosphate buffer with a pH of 7.5 containing $[Fe(CN)_6]^{3-/4-}$. A Ag/AgCl electrode was used as a reference electrode to control the cell potential and the flow of electrons in the phosphate buffer. The third electrode, known as the counter electrode, was a Pt electrode resistant to oxidation. The B-MgO NP/ITO bioelectrode was used for the detection of Vit-B_{12}, which is a water-soluble cobalt compound with variable oxidation states between Co^{2+} and Co^{3+} ions. The overall internal reaction between the B-MgO NP/ITO electrode, the mediator $Fe^{2+/3+}$ ions, the $Co^{2+/3+}$ ions of Vit-B_{12}, and the function of the three electrodes are depicted in Fig. 2.

2.5. Characterization

The structural and morphological characterization of B-MgO NPs was performed through combination of several techniques. UV-vis spectroscopy (Agilent Cary 60 UV-vis) was used to confirm the absorbance, conducting and non-conducting

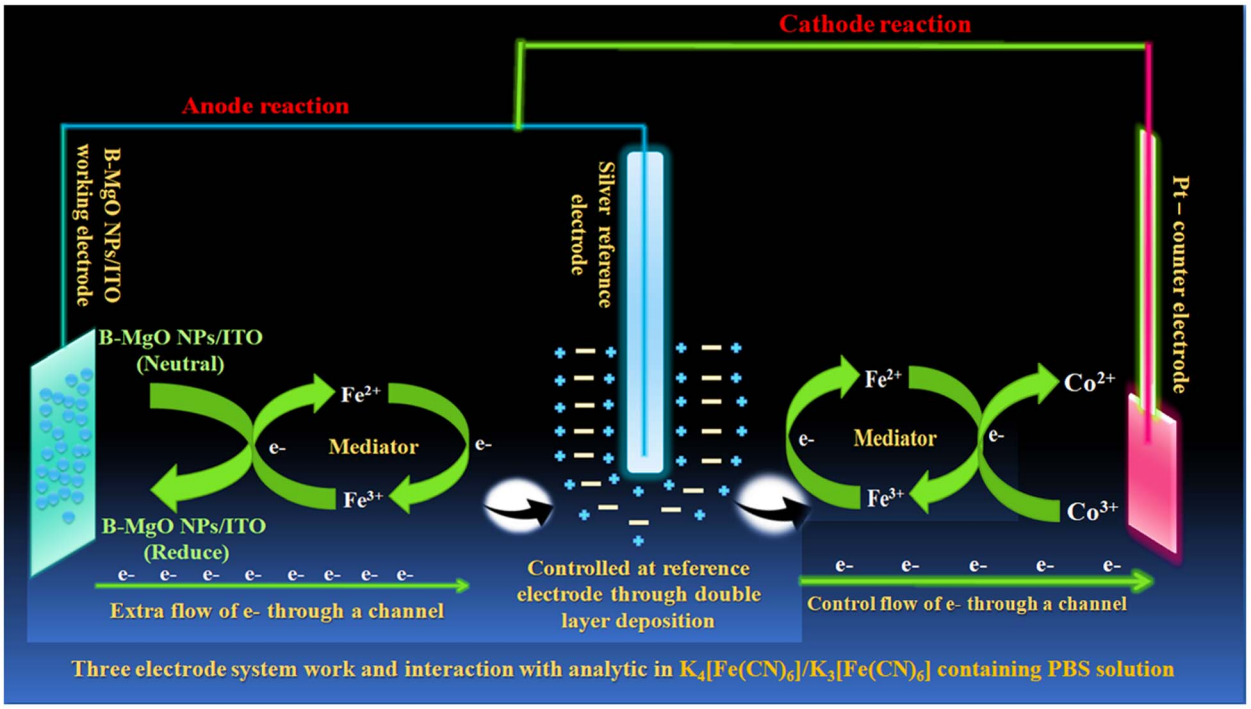

Fig. 2 Schematic illustration of Vit-B_{12} detection in phosphate buffer containing $[Fe(CN)_6]^{3-/4-}$ and the working three-electrode system.

behavior. FTIR-spectroscopy (modal FTIR 4700 make: JASCO, TOKYO) provided information of the available functional groups. XRD (D8-ADVANCE(eco)/(Bruker)) corrected the information of the crystalline shape, structure and size. AFM (NT-MDT model-solver Next) showed the 3D and 2D images, and the roughness of the surface. XPS (PHI 5000 Versa Probe (III) (scanning XPS microprobe)) provided information on the particular elements and corresponding binding energies. SEM and EDX (Carl Zeiss company instrument; model EVO-18 Research) sample preparation coating was achieved through spattering of Au on the B-MgO NPs and using a source laser and lanthanum hexaboride (LaB_6). SEM confirmed the morphology, size, and high-quality 3D image, and EDX confirmed the presence and percentages of different elements in the compound. TEM HR-TEM and SAED (Techai G^2 20 TWIN, FEI company of USA) confirmed the particle size, shape, *d*-spacing between planes, and the crystalline and amorphous nature. The electrochemical analysis of B-MgO NPs was performed by the instrument electrochemical workstation Corrtest CS studio 350. An ITO (resistivity-20 Ω sq^{-1}) electrode was used as the working electrode for the fabrication of the biosensor.

3. Results and discussion

3.1. Structural analysis of B-MgO NPs

3.1.1. Powder XRD analysis. The powder X-ray diffraction (PXRD) analysis shown in Fig. 3(a) confirmed the crystalline system and phase of B-MgO NPs. The PXRD of B-MgO NPs exhibits peaks at 37°,43°, 62°, 74° and 78°, corresponding to the (111), (200), (220), (311) and (222) planes with *d*-spacings of 2.4, 2.1, 1.4, 1.2 and 1.2 nm (JCPDS No-897746), respectively.[41] They confirm that the B-MgO NPs have a perfect cubic crystal system with a face-centered cubic type lattice close packing. Here, Mg^{2+} is bonded to six equivalent O^{2-} atoms, occupying the corner and edge-sharing MgO_6 octahedral platform. A PXRD pattern shows a highly intense orientation peak (200), confirming the pure phase and high crystallinity of B-MgO NPs.[42] The average crystalline size can be calculated by the Debye Scherrer (eqn (2)).

$$D = \frac{0.9\lambda}{\beta \cos \theta} \quad (2)$$

In this equation, D corresponds to the crystallite size, where λ is the wavelength of the X-ray source Cu Kα radiation, β is the full-width at half-maxima (FWHM) of the most intense peak (β = 0.0164) and θ is the Bragg diffraction angle.[43] The average crystallite size of B-MgO NPs has been calculated as 9.08 nm.

3.1.2. FTIR analysis. FTIR (Fourier Transforms Infrared) spectroscopy analysis of B-MgO NPs is shown in Fig. S1(a),† and was performed in the range of 500–4000 cm^{-1}, confirming various functional groups. The B-MgO NPs showed detectable peaks at 3430, 1462, 1097, 870, 642 and 482 cm^{-1} for various functional groups. The strong broad peak at 3430 cm^{-1} indicates the presence of a stretching vibration of the hydroxyl group.[41] The sharp peaks at 1462 cm^{-1} and 1097 cm^{-1} relate to the bending vibration of the hydroxyl group.[42] The intense peak observed at 870 cm^{-1} confirms the presence of MgO, along with the O–C=O group of biomolecules.[44] The two sharp peaks at 642 cm^{-1} and 482 cm^{-1} are the stretching and bending vibrations of Mg–O, respectively, and may confirm the formation of the metal oxide bond.[44] Balakrishnan *et al.* investigated the MgO nanoparticles using FTIR spectroscopy and identified a vibration peak corresponding to the O–Mg–O bond at

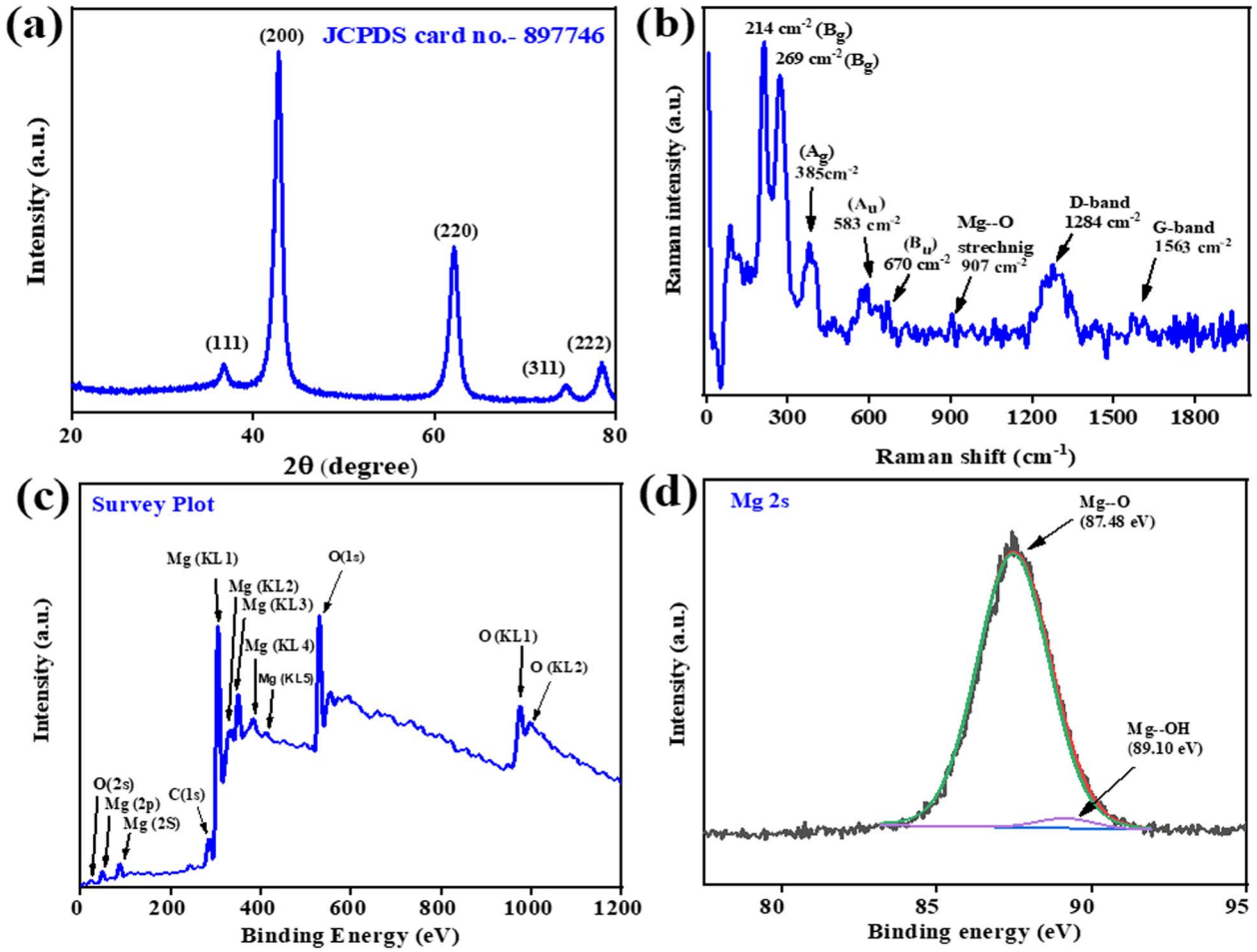

Fig. 3 The (a) XRD spectra of B-MgO NPs in the 2θ range of 20–80°. (b) Raman spectra of different modes of B-MgO NPs; (c) XPS survey spectra and (d) Mg (2s) XPS spectra of B-MgO NPs.

approximately 600–850 cm^{-1}. Additionally, a broad band around 3268 cm^{-1} was observed, indicating the stretching of hydroxyl groups on the surface of the nanoparticles, likely due to moisture.[45]

3.1.3. UV spectroscopy. The formation of B-MgO NPs was confirmed by Ultraviolet (UV) spectroscopy detection, as shown in Fig. S1(b).† The UV spectra have been plotted between the absorbance and wavelength (range 200–800 nm). In this regard, Hassan *et al.* reported on the micro-synthesized MgO NPs maxima from surface plasmon resonance (SPR) at 282 nm.[46] Furthermore, Aghebati-Maleki *et al.* reported on the UV absorption spectra in the 220–650 nm region without a maxima of the chemically-synthesized MgO NPs.[47] The present data are compatible with the previously reported B-MgO NPs showing a distinctive absorption band of MgO up to 800 nm. There are no sharp peak observed, confirming that the nanoparticles are of different sizes.[48] Furthermore, the UV spectra of B-MgO NPs were used to calculate the energy band gap (E_g) value by Tauc's relation, as expressed in the following formula (eqn (3)):

$$(ahv)^2 = A(hv - E_g) \quad (3)$$

where, h is Planck's constant, A is a constant, α is the absorption coefficient, and E_g is the energy band gap. To calculate the energy band gap, Tauc's equation curve in Fig. S1(c)† was extrapolated and an energy band gap of 5.6 eV was observed.[49] This band gap should have low conducting properties, but the increasing electrostatic potential on the surface of the nanosheet due to the presence of π electrons from the p-orbital resulted in a transition to the Fermi level. Due to this transition, B-MgO NPs should be conducting.[50] Nelson *et al.* reported on a MgO nanoparticle band gap at 5.8 eV.[51] These results confirm that the B-MgO NPs surface ions are involved in electron transfer *via* incident UV radiation. It shows a conceivable reaction, which is presented in eqn (4).[49]

$$Mg^{2+}O^{2-} + hv^- \rightarrow Mg^{+}O^- \quad (4)$$

Fermi levels reduced the energy gap for a suitable transition of electrons from the lower energy level to higher energy levels, as well as enhanced conductivity with a 5.6 eV non-conducting band of B-MgO NPs.

3.1.4. Raman spectroscopy. Raman spectroscopy introduces the structural and compositional information with bond vibration and stretching properties of B-MgO NPs. Fig. 3(b) exhibits the

sharp, intense peaks at 1563, 1284, 907, 670 (B_u), 583 (A_u), 385 (A_g), 269 (B_g), and 214 (B_g) cm^{-1}. Chen *et al.* defined the magnesium oxide nanoparticle Raman- and IR-active modes of different frequencies, their corresponding irreducible representations, and point groups. Based on the previously reported data and similarity with the defined spectra reported herein, the collective results defined the samples as $(MgO)_{3n}$ ($n = 4$) with C_{2h} point group, introducing four modes such as A_g, A_u, B_g and B_u. A_g and B_g are Raman-active modes, and A_u and B_u are IR-active modes. Meanwhile, one mode is neither Raman-active nor IR-active due to the significant figure of computation.[52] The Raman band at 907 cm^{-1} represents the Mg–O bond stretching vibration in B-MgO NPs. Boyadjian *et al.* promoted the Li/MgO catalyst properties with a variable amount of MgO NPs for the oxidative conversion of *n*-hexane, which was confirmed through a Raman study. They precisely described the MgO stretching vibration of the Mg–O bond as represented by a sharp peak at 908 cm^{-1}, and the Raman shifting with a variable amount of MgO NPs.[53] The G-band appearing in the 1550–1600 cm^{-1} range is attributed to the tangential modes (E_g) of the vibration of sp^2 bonded C atom. Hussain *et al.* reported a new band at 1250 and 1440 cm^{-1}, attributed to the mixed vibration of C≡C and C–C, associated with a reduced tip distance of 2.5 Å. This band complements the observation of non-uniform amorphous carbon in the green rough, evident in the 1280–1430 cm^{-1} range attributed to the D-band.[54] These spectra matched the previously reported MgO NPs; thus, it can be concluded that the B-MgO NPs have a C_{2h} point group with two Raman-active and two IR-active modes.

3.1.5. XPS analysis. X-ray photoelectron spectroscopy (XPS) is used to detect the oxidation state, valence state, composition, and empirical formula of elements. The XPS survey spectra of B-MgO NPs are shown in Fig. 3(c) in the 0–1200 eV binding energy region. The Mg, O, and additional impurity of the organic contaminant green material carbon are present in the B-MgO NPs. Magnesium reveals different binding energies of different species of magnesium, like Mg (2s), Mg (2p), Mg (KL1), Mg (KL2), Mg (KL3), Mg (KL4) and Mg (KL5). Oxygen of B-MgO NPs shows different binding energies like O (2s), O (1s), O (KL1) and O (K110L2), as well as carbon.[46] Carbon is also revealed in the survey spectra, showing the binding energy of C (1s).[55] The deconvoluted spectra of Mg was fitted in the Shirley-type background in XPS 4.1 software. Fig. 3(d) shows the asymmetric XPS spectra of the Mg (2s) orbital, which is the Shirley-type fit in the 83–91 eV range of the imported DAT file, and the background fitting of the possible binding energies. After the complete fit procedure, exporting of the ASCII file, and saving the deconvoluted file, the plot in Origin software shows two peaks at 87.48 eV and 89.10 eV from MgO and $Mg(OH)_2$, respectively.[46] The same fit procedure was done with the oxygen and carbon elements. Furthermore, O 1s in Fig. S1(d)† shows that the asymmetric XPS spectra could be deconvoluted into two peaks at 528.30 eV and 530.25 eV.[56] They may be ascribed to the lattice oxygen of MgO and $Mg(OH)_2$, respectively.[57] Fig. S1(e)† shows the asymmetric XPS spectra of C 1s, which could be deconvoluted into two peaks at 283.35 eV and 288.53 eV of C–C and C–O, respectively.[55] The XPS analysis of B-MgO NPs has briefly introduced the preponderance of the formation of MgO with an evidential amount of $Mg(OH)_2$.

3.1.6. Atomic force microscopy. Atomic Force Microscopy (AFM) of B-MgO NPs confirmed the texture of the thin film and its surface morphology. Fig. 4(a) shows the topographic 2D image of B-MgO NPs, wherein the highlighted bright spherical shape spots represent the B-MgO NPs crystallites grown relative to the grain morphology. This result indicates that the B-MgO NPs are uniformly deposited into the ITO surface, forming a precise platform for the electrochemical biosensing of Vit-B_{12} by B-MgO NPs. Fig. 4(b) is the 3D-image of the faceted columnar microstructure, representing the roughness of the B-MgO NPs. Fig. 4(c) is the histogram of the 3D image, confirming that the root mean square roughness (Sq), average roughness (Sa) and maximum area of the peak height are 1.756, 1.411 and 7.590 nm, respectively.[58]

3.1.7. SEM and EDX analysis. Scanning electron microscopy (SEM) was used to obtain a high-quality image of the surface morphology of B-MgO NPs. SEM confirmed the nanoflake-like structural images of B-MgO NPs, as presented in Fig. 4(d and e). These results indicate that the average particle size is probably in the 1 μm and 2 μm range. The aggregation of several nanoparticles introduced the nano cornflakes structure of B-MgO NPs.[25] Auxiliary information of the characteristic elemental composition of the B-MgO NPs was confirmed by energy dispersive X-ray (EDX) spectroscopy. The existence of Mg, O and C elemental peaks is shown in Fig. 4(e), and confirm the purity of the B-MgO NPs. Here, the extra elemental peak shows the growing existence of the green material. The atomic percentage and weight percentage of the individual element are affixed with the EDX spectra plot.[1] The atomic percentage (%) and weight percentage (%) of Mg, O, and C are 20.08, 12.73, 47.69 and 45.93, 32.23, 41.34, respectively. No peak observed in the spectra demonstrates the purity of B-MgO NPs.

3.1.8. TEM spectroscopy. Transmission electron microscopy (TEM) and high-resolution transmission electron microscopy (HR-TEM) images revealing the particles in the nano-range are shown in Fig. 4(f and g). The morphology, crystalline and amorphous, size of the particles and *d*-spacing, and properties of B-MgO NPs can be observed. Herein, we introduce the 200 nm and 10 nm range resolution images, which reveal the overlapping of several spherical B-MgONPs.[59] Fig. 4(g) shows the HR-TEM interplanar lattice fringes of the corresponding *d*-spacing. These *d*-spacings are confirmed by JCPDS card number 897746 with the approximate accurate results of the corresponding PXRD. At the obtained planes (111), (200), (220), (311) and (222), the *d*-spacing is 0.24, 0.21, 0.14, 0.12 and 0.12 nm, respectively, which were calculated through the ImageJ software. Fig. 4(h) is the Selected Area Electron Diffraction (SAED) pattern, showing the crystallographic image of B-MgO NPs. The SAED pattern shows clear, dark, visible rings of diffracted light beams, which confirm that the highly peaked crystals were formed and also gives information of the interplanar distance, *i.e.*, *d*-spacing. The average particle sizes of the B-MgO NPs were confirmed through the histogram fitting by Lorentzian function. A histogram plot of B-MgO NPs has been inserted in Fig. 4(i), which shows that the average particle size is 17.17 nm, confirming that the nano-sized particle has been formed. These

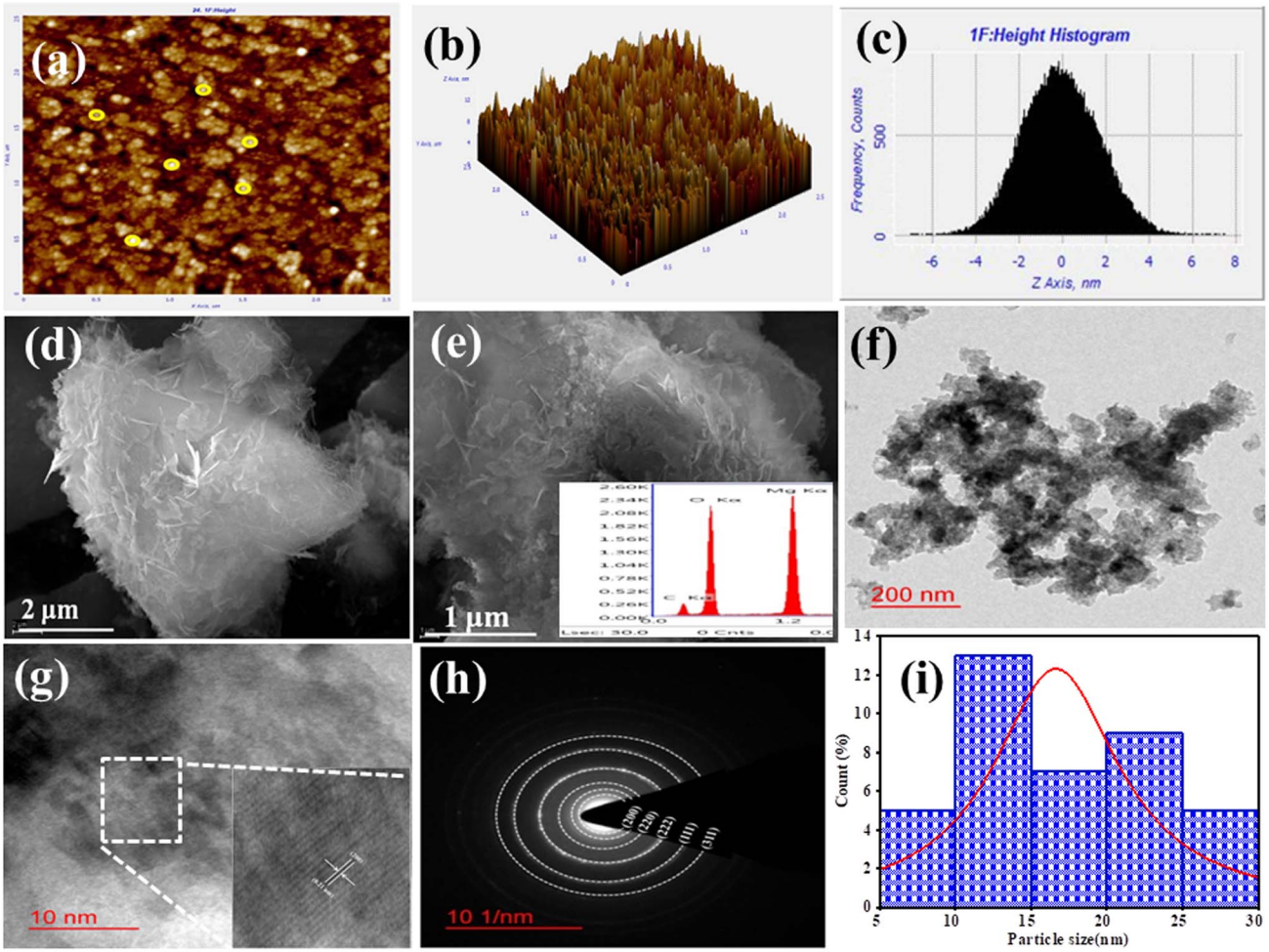

Fig. 4 Morphological characterization of B-MgO NPs. AFM images showing the (a) 2D-image, (b) 3D-image, and (c) height peak profile. SEM image of (d) 2 µm and (e) 1 µm; inset shows the EDX plot of elements. (f) TEM micro-image at 200 nm and (g) 10 nm HR-TEM image and the inset is the magnified image of fringes; (h) SAED pattern and (i) histogram plot of the particle size.

results correlate with the average crystalline size of 9.08 nm verified through PXRD.[43] These HR-TEM and SAED patterns clearly show the mono-crystalline nature of B-MgO NPs, with different diffraction planes including (111), (200), (220), (311) and (222). These diffraction planes are confirmed through the PXRD pattern and reveal the cubic structure of B-MgO NPs.[60]

4. Electrochemical study

4.1. CV and DPV study

The electrocatalytic behavior of the B-MgO NP/ITO bioelectrode has been confirmed by cyclic voltammetry (CV). These CV studies of the modified B-MgO NP/ITO bioelectrode were performed in $[Fe(CN)_6]^{3-/4-}$ containing phosphate buffer (5 mM, 0.9% NaCl) at a scan rate of 50 mV s^{-1} in the potential range of −0.8 V to 1.0 V (Fig. 5(a)). A comparative cyclic voltammogram (CV) study of the conducting bare ITO and modified B-MgO NP/ITO bioelectrode in $[Fe(CN)_6]^{3-/4-}$ mediator exhibited an oxidative peak current density (I_{pa}) of 0.97 mA cm^{-2} and 1.03 mA cm^{-2}, respectively. The resultant peak current density of the modified B-MgO NP/ITO bioelectrode is higher than that of the bare ITO. This is due to the high electrochemical conductivity, large surface area, and superior catalytic behavior of the modified B-MgO NP/ITO bioelectrode compared to the bare ITO for the detection of Vit-B_{12}. The reductive peak potential (E_{pc}) of 0.03 V and oxidative peak potential (E_{pa}) of 0.37 V were shown by the B-MgO NP/ITO bioelectrode. The catalytic behavior and high electrochemical conductivity of the B-MgO NPs were validated by differential pulse voltammetry (Fig. 5(b)).

4.2. Scan rate and kinetic study of the B-MgO NP/ITO bioelectrode

The interfacial kinetics of the B-MgO NP/ITO bioelectrode was explored by CV study of the scan rate, and a redox peak was observed in the range of 10 to 100 mV s^{-1} as shown in Fig. 5(c). That distinguishable magnitude linearly increases with the square root of the scan rate ($\nu^{1/2}$) of the anodic (I_{pa}) and cathodic (I_{pc}) peak current densities (Fig. 5(d)). The CV curve of the scan rate shows a continuously enhanced oxidation peak, as well as

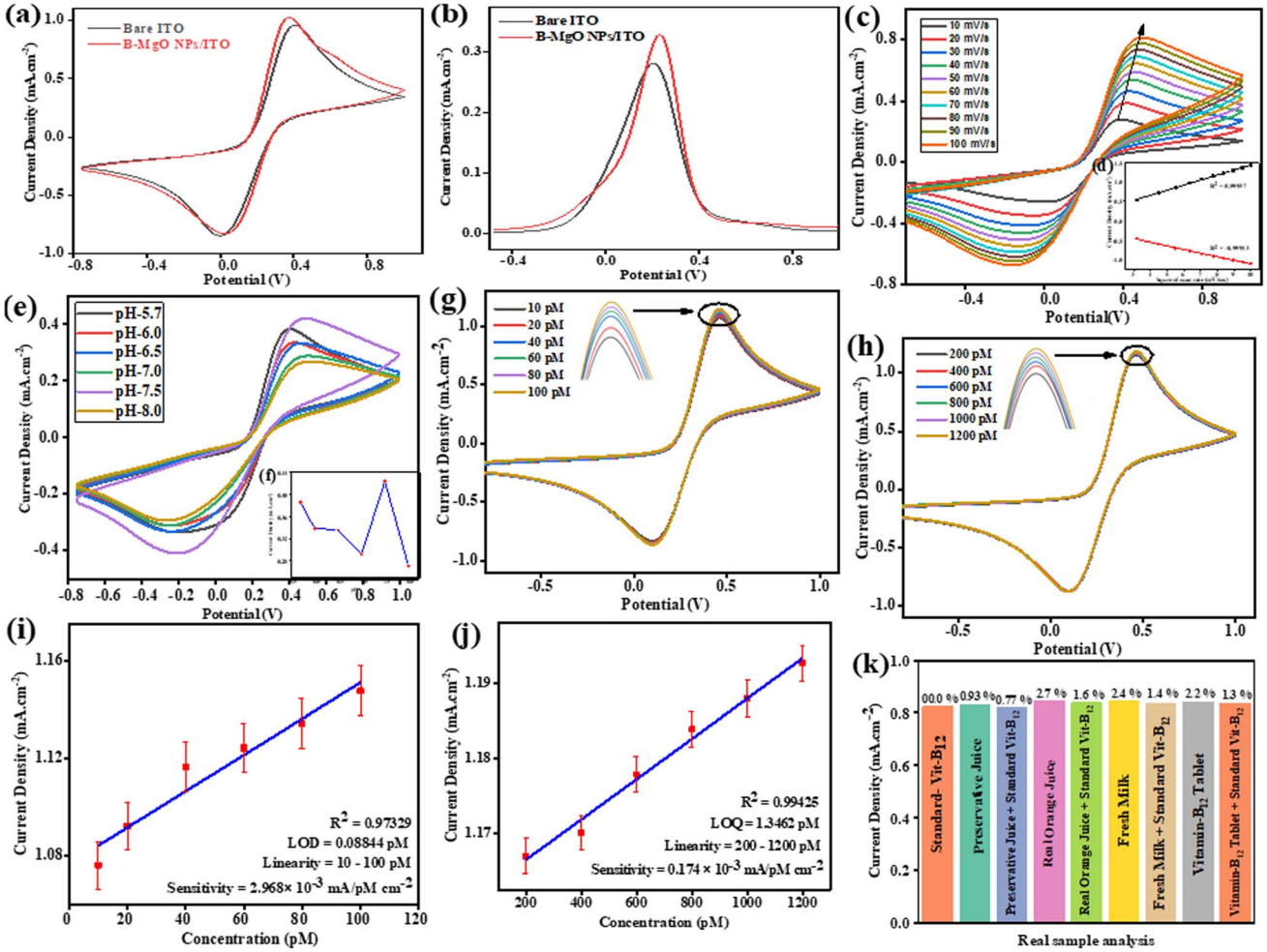

Fig. 5 Cyclic voltammetry studies of the B-MgO NP/ITO bioelectrode in $[Fe(CN)_6]^{3-/4-}$ containing phosphate buffer (0.9% NaCl, pH 7.5) at a scan rate of 50 mV s^{-1} in the potential range of −0.8 to 1.0 V. (a) CV study of the bare ITO and B-MgO NP/ITO bioelectrode. (b) DPV study of the bare ITO and B-MgO NP/ITO bioelectrode. (c) CV study of the scan rate and ((d), inset of (c)) relative calibration plot of the current density *vs.* square root of the scan rate ($v^{1/2}$). (e) pH (5.7–8.0) range studies *via* CV, and ((f), inset of (e)) linear fit curve of the pH sensitivity of the B-MgO NP/ITO bioelectrode towards Vit-B_{12}. Linearity in sensitivity towards (g) 10–100 pM concentration and (h) 200–1200 pM concentration, while (i) and (j) are the respective calibration curves for (g) and (h). (k) Bar graph from the Vit-B_{12} analysis of a real sample using the B-MgO NP/ITO bioelectrode.

a shifting of the reductive peak towards more positive and negative directions, respectively; thus, this redox process is quasi-reversible. By the linearity relation of the electrochemical reaction between the electrode and electrolyte, it is concluded that this process is a diffusion-controlled process rather than adsorption. The Laviron equation (eqn (5))[61]-verified surface modification can be confirmed by the charge transfer rate constant (K_S):

$$K_s = \frac{mnFv}{RT} \quad (5)$$

where F is the Faraday constant (96 500 C mol^{-1}), m is the peak-to-peak separation (V), n is the number of transferred electrons (1), R is the gas constant (8.314 J K^{-1} mol^{-1}), v is the scan rate (50 mV s^{-1}), and T is the temperature (25 °C). The surface physiochemistry and electronic structure of the B-MgO NPs were shown to increase *via* calculated K_S (1.071 s^{-1}) of the B-MgO NP/ITO bioelectrode. This enhanced electron transfer is due to the high catalytic behavior of the B-MgO NPs.

The linearity relation of the scan rate of the cathodic peak potential (E_{pc}), anodic peak potential (E_{pa}), and difference in the peak shift potential ($E_P = E_{pa} - E_{pc}$) have shown that the process is diffusion-controlled.[62] The diffusion coefficient (D) of the tunable electrons between the electrolytic solution ($[Fe(CN)_6]^{3-/4-}$) and electrode surface of the B-MgO NP/ITO bioelectrode has been calculated by the Randles–Sevcik equation (eqn (6)).

$$I_p = (2.69 \times 10^5) n^{3/2} A D^{1/2} C v^{1/2} \quad (6)$$

where I_{pa} is the anodic peak current and I_{pc} is the cathodic peak current, I_p is the peak current density of the relative electrode, A is the surface area (0.25 cm^2) of the electrode, C is the surface concentration in mol (5 mM), n is the number of electrons (1), D is the diffusion coefficient and v is the scan rate (50 mV s^{-1}). The value of D for the B-MgO NP/ITO bioelectrode is 0.149 cm^2 s^{-1}.

The Brown–Anson model equation (eqn (7))[63] can be used to estimate the surface concentration of the B-MgO NPs on the electrode.

$$I_p = \frac{n^2F^2I^*Av}{4RT} \quad (7)$$

where F is the Faraday constant, R is the gas constant (8.314 J K^{-1} mol^{-1}), n is the number of electrons (1), I^* is the surface concentration of the corresponding electrode (mol cm^{-2}), A is the surface area of the electrode (0.25 cm^2), v is the scan rate (50 mV s^{-1}), and T is the temperature (25 °C). The observed surface concentration (I^*) of the B-MgO NP/ITO bioelectrode is 0.557 mol cm^{-2}.

4.3. pH optimization

The electrochemical behavior of the B-MgO NP/ITO bioelectrode has been studied in the physiological range of pH 5.7–8.0, confirming the effect of the solution. The continuous solution effect on the B-MgO NPs has been measured by cyclic voltammetry (CV) technique in $[Fe(CN)_6]^{3-/4-}$ containing phosphate buffer (5 mM, 0.9% NaCl) at a scan rate of 50 mV s^{-1} in the potential range of −0.8 to 1.0 V. Fig. 5(e and f) shows the maxima of the physiological range of pH observed at pH 7.5. Its attribute is most probably due to the limited electron flow between the electrode and medium. These results confirmed the decrease in E_{pa} with the simultaneously increase in the current density at pH 7.5. The cyclic voltammetry study of the B-MgO NP/ITO bioelectrode presented the redox reaction and simultaneous electron flow between $Mg^{2+/1+}$ of the bioelectrode and $[Fe(CN)_6]^{3-/4-}$ of PBS. It was found that pH 7.5 is the best buffer condition for the redox reaction of the B-MgO NP/ITO bioelectrode and $[Fe(CN)_6]^{3-/4-}$ of the phosphate buffer.

4.4. Electrochemical response study of Vit-B_{12} on the fabricated B-MgO NPs bioelectrode

An electrochemical response study was performed for the B-MgO NP/ITO electrode for investigating Vit-B_{12}. A current density have been linearly increases with an increase Vit-B_{12} concentration from 10 to 100 pM and 200 to 1200 pM at 50 mV s^{-1} scan rate (−0.8 to 1.0 V) using CV technique, as shown in Fig. 5(g and h). The current density continuously increased with the addition of 20 μmL Vit-B_{12} of each concentration range because the electrode/electrolyte interface increases the concentration gradient, and the oxidation and reduction of Vit-B_{12} take place simultaneously at the electrode. The continuous increase in the a concentration gradient with current density has been attributed to the thickness of the diffusion layer with increasing time. The relationship between the magnitude of the peak current density with different concentrations of Vit-B_{12} is shown in the calibration curve in Fig. 5(i and j).

A good linearity was observed in the 10 pM to 100 pM range with $R^2 = 0.973$, and in the 100 pM to 1200 pM range with $R^2 = 0.994$. The limit of detection (LOD) and limit of quantification (LOQ) were calculated by eqn (8) and (9), respectively. The sensitivity of the fabricated bioelectrode was found to be 2.96×10^{-3} and 0.17×10^{-3} mA pM^{-1} cm^{-2}.

$$LOD = \frac{3 \times SD}{\text{sensitivity}} \quad (8)$$

$$LOQ = \frac{10 \times SD}{\text{slope}} \quad (9)$$

where S is the sensitivity which is calculated by the difference between the slope and area of the electrode, and σ_1 and σ_2 represent the standard deviation of the low and high concentrations of Vit-B_{12}. The LOD and LOQ for the B-MgO NP/ITO electrode are 0.088 pM and 1.346 pM, respectively. Table 2 presents a summary of the previously reported synthesized nanomaterials, fabrication of the electrochemical Vit-B_{12} biosensor, and sensitivity toward Vit-B_{12}.

4.5. Reusability test of the fabricated B-MgO NP/ITO bioelectrode

Reusability of the B-MgO NP/ITO bio-electrode was investigated at 200 pM concentration of Vit-B_{12}, by taking **9** repetitive measurements of the current density, as shown in Fig. S2(a and b).† The response was measured in regular time intervals of 5 s, in $[Fe(CN)_6]^{3-/4-}$ containing phosphate buffer (0.9% of NaCl, pH 7.5, 50 mM). Reusability of the B-MgO NP/ITO bioelectrode was retained at **6** scans. However, after that, the current density gradually decreased. The RSD value at 2, 3, 4, 5, 6, 7, 8 and 9 scans with respect to the first scan is 0.001%, 0.00%, 0.065%, 0.22%, 2.81%, 4.08%, 4.56% and 4.95%, respectively. These show that there is only a slight change in the RSD value until 6 scans; after that, the RSD value gradually increases. This confirms that the investigated B-MgO NP/ITO is reusable for 6 scans with an approximate 0% to 5% RSD value.

4.6. Stability of the fabricated electrode

The stability of the B-MgO NP/ITO bio-electrode was monitored *via* CV at a regular time interval of 5 days in $[Fe(CN)_6]^{3-/4-}$-containing phosphate buffer (0.9% NaCl, pH 7.5, 50 mM), as shown in Fig. S2(c and d).† The B-MgO NP/ITO bioelectrode maintained activity for up to 20 days, demonstrating its stability (Fig. S2(d)†). The stability of the B-MgO NP/ITO bioelectrode depends on the physiologically integrated stability of the B-MgO NPs material on ITO, which affects the response of the current density. Results indicate that the B-MgO NP/ITO bioelectrode was stable for 20 days at 4 °C, demonstrating the long lifetime and excellent storage capacity of the B-MgO NP/ITO bioelectrode towards Vit-B_{12} detection.

4.7. Response time

The response time of the B-MgO NP/ITO bioelectrode was performed in Vit-B_{12} at 200 pM concentration, as shown in Fig. S2(e and f).† During the CV measurement for a total of 60 s with 5 s regular time intervals (Fig. S2(e)†), the current density gradually increased until 45 s and remained steady from 45 to 50 s, and then continuously decreased until 60 s (Fig. S2(f)†). This sensor achieved 99.63% of the steady state current density in less than 45 s, indicating that the B-MgO NP/ITO bioelectrode has excellent conductivity towards Vit-B_{12} detection.

Table 2 Comparative sensing performances of the B-MgO NP/ITO bioelectrode with other recently reported materials for the detection of Vit-B_{12}

				Results						
S. no.	Sensing materials	Technique	Range of detection	Sensitivity	Stability	Reusability	Response time	LOD	pH	Ref.
1	Cu(HBTC) (4,4′-bipy) 3DMF nano-electrode/ platinum electrode	Cyclic voltammetry	100–188, 200 nM	0.104 nM	2 weeks	10 times	—	50 nM	3	64
2	Polymer of [Mn(thiophenyl-2-carboxylic acid)$_2$(triethylonamine)] peptide nanotube/carbon paste	Square wave voltammetry (SWV)	2.7–174 nM	18.02 nM				0.97 nM		65
3	Gold/polypyrrole/ ferromagnetic nanoparticle/triazine dendrimer [Au/PPy/ FMNPs@TD] electrode	Cyclic voltammetry (CV)	4.0–500 nM	25.6 μA nM^{-1} cm^{-2}	—	—	—	0.62 nM	7.0 (Britton–Robinson buffer)	4
4	Copper oxide nanocrystal graphenic composite electrode	Electrochemical study (CV, LSV)	0.15–7378 nM	—	—	—	6, 9, 12, 15, 18 and 21 min	0.59 nM	7.0 (neutral)	6
5	Au-SnO_2/ITO electrode	Electrochemical impedance spectroscopy (EIS)	0–1500 pM	—	—	—	20 min	71.48 pM	7.0 (phosphate buffer solution-PBS)	1
6	Pd Au-PPy/CFP electrode (CFP- carbon fiber electrode)	Cyclic voltammetry (CV)	4.01–52.5 pM (MMA)	10 576 μA nM^{-1} cm^{-2}	30 days	40 times	—	1.32 pM	7.0 (PBS)	24
7	PNT/PGE (peptide nanotube/pencil graphite electrode)	Square wave voltammetry (SWV)	200–9500 μM	—	—	—	—	0.093 pM	2 (PBS)	29
8	B-MgO NP/ITO	Cyclic voltammetry (CV)	10–100 pM and 200–1200 pM	2.968×10^{-3} and 0.174×10^{-3} mA pM^{-1} cm^{-2}	20 days	9 times	45 s	0.088 pM and 1.346 pM	7.5 (PBS)	This work

Table 3 Results of real sample analysis using the fabricated B-MgO NP/ITO electrode

S. no.	Real sample detection	Concentration of real sample	Recovery percentage	RSD
1	Standard vitamin-B_{12}	200 pM	100%	0.00%
2	Preservative juice	201.87 pM	100.93%	0.93%
3	Preservative juice + standard vitamin-B_{12}	198.35 pM	99.17%	0.83%
4	Real orange juice	205.58 pM	102.79%	2.79%
5	Real orange juice + standard vitamin-B_{12}	203.34 pM	101.67%	1.67%
6	Milk	204.94 pM	102.47%	2.47%
7	Milk + standard vitamin-B_{12}	202.90 pM	101.45%	1.45%
8	Tablet-vitamin-B_{12} +	204.40 pM	102.20%	2.20%
9	Tablet-vitamin-B_{12} + standard vitamin-B_{12}	202.70 pM	101.35%	1.35%

4.8. Interference study

The influence of interference on the transducer signal was investigated in $[Fe(CN)_6]^{3-/4-}$-containing phosphate buffer (0.9% NaCl, pH 7.5) at a scan rate of 50 mV s^{-1} in the potential range of −0.8 to 1.0 V, as shown in Fig. S2(h).† The conversion of the electrochemical current density was measured in phosphate buffer containing an equal amount (1 : 1) of standard vitamin-B_{12} (200 pM/20 μL), along with a normal physiological concentration of different interferents, such as vitamin-B_2 (40 μM/20 μL), vitamin-C (20 μM/20 μL), glucose (500 μM/20 μL), lactic acid (100 μM/20 μL), glutamic acid (500 μM/20 μL), urea (40 μM/20 μL), and vitamin-D_3 (500 μM/20 μL). The interference study of Vit-B_{12} has been performed in Vit-B_2 (1%), Vit-C (11%), glucose (6%), lactic acid (8%), glutamic acid (6%), urea (8%), Vit-D_3 (5%) and the mixture (6%) shows the % RSD, respectively, with the approximation ±11% change.

4.9. Real sample analysis

The performance of the fabricated B-MgO NP/ITO bioelectrode electrochemical biosensor in detecting Vit-B_{12} was examined in real samples. The analysis of a real sample was performed on the modified B-MgO NP/ITO bioelectrode in a $[Fe(CN)_6]^{3-/4-}$ containing phosphate buffer (0.9% NaCl, pH 7.5) at a scan rate of 50 mV s^{-1} in the potential range of −0.8 to 1.0 V. The distinguishable deviation in the electrochemical current density response was measured in phosphate buffer with the same quantity of the standard Vit-B_{12} (200 pM/20 μL), along with real samples (undisclosed concentration/20 μL), such as preservative juice, real orange juice, fresh milk, and vitamin-B_{12} tablet. Fig. 5(k) shows the bar graph of the real sample analysis between the current density and a real sample concentration, such as standard Vit-B_{12}, preservative juice, real orange juice, fresh milk, vitamin-B_{12} tablet, and the % RSD values are indicated in Table 3. This relative % RSD approximation ±3% change value confirmed that the B-MgO NP/ITO biosensor shows less fluctuation in the current density in the real sample. The undisclosed concentration of Vit-B_{12} in the real sample was confirmed, as determined by the standard current density with respect to the real current density and standard concentration (200 pM). The undisclosed concentration of the real samples was revealed with respect to the standard concentration (200 pM), showing the percentage recovery (%) in the preservative juice, real orange juice, fresh milk, and vitamin-B_{12} tablet represented in Table 3. The results of the real sample analysis confirmed that the prepared B-MgO NP/ITO biosensor was selective toward Vit-B_{12} in $[Fe(CN)_6]^{3-/4-}$-containing phosphate buffer (0.9% NaCl, pH 7.5) at a scan rate of 50 mV s^{-1} in the potential range of −0.8 to 1.0 V.

5. Conclusion

In summary, B-MgO NPs were successfully synthesized using a green route hydrothermal method with Kachnar (*Bauhinia Variegata*) flower extract. The synthesis was confirmed through various optoelectronic characterization techniques, such as UV-vis, FTIR, XRD, XPS, AFM, SEM, TEM, and HR-TEM. Analysis of the XRD and TEM data revealed an average crystalline size of 9.08 nm, which is smaller than the average particle size of 17.17 nm. To explore its potential for Vit-B_{12} detection, a thin and uniform layer of B-MgO NPs was electrophoretically deposited onto an ITO substrate. The modified B-MgO NP/ITO bioelectrode exhibited enhanced conductivity compared to bare ITO, as confirmed by CV and DPV studies. Scan rate studies indicated a high catalytic behavior (Ks) of 1.071 s^{-1}, a diffusion coefficient (D) of 0.1496 cm^2 s^{-1}, and a surface concentration (I^*) of 0.5572. The sensitivity of the modified B-MgO NP/ITO bioelectrode was determined to be 2.968 × 10^{-3} mM pM^{-1} cm^{-2} in the range of 10 to 100 pM, and 0.174 × 10^{-3} mM pM^{-1} cm^{-2} in the range of 100 to 1200 pM. The B-MgO NP/ITO bioelectrode demonstrated high accuracy for Vit-B_{12} detection, with a limit of detection (LOD) of 0.088 pM and a limit of quantification (LQD) of 1.346 pM. Moreover, the B-MgO NP/ITO bioelectrode exhibited stability for up to 20 days and reusability for up to 9 times with regular 5 second intervals. It also showed a better response time of 45 seconds, with ±6% interface interaction and ±3% acceptable percentage error in real sample studies. The fabrication process using the green route ensured the biodegradability, biocompatibility, reusability, selectivity, sensitivity, and specificity of the B-MgO NP/ITO bioelectrode for Vit-B_{12} detection.

Author contributions

S. S.: data curation, investigation, visualization, writing – original draft. R. V.: validation, data curation, and writing – original

draft. K. R. B. S: data curation, validation, visualization, writing – review & editing of original draft. J. S.: conceptualization, resources, validation, project administration, supervision, writing – review & editing of original draft.

Conflicts of interest

The authors declare that they have no known competing financial interests or personal relationships that could have appeared to influence the work reported in this paper.

Acknowledgements

This work received no specific grant from public, commercial, or not-for-profit funding agencies. S. S. and R. V. are thankful to their affiliated institution for providing constant financial support. K. R. B. S. is grateful to BHU (IoE grant project) for financial support throughout this work. Author J. S. acknowledges BHU for providing a seed grant and BRIDGE grant under MoE Govt. India, Institute of Eminence (IoE), under Dev. Scheme No. 6031 & 6031A respectively.

References

1 A. Sharma, S. Arya, D. Chauhan, P. R. Solanki, S. Khajuria and A. Khosla, *J. Mater. Res. Technol.*, 2020, **9**, 14321–14337.
2 J. Gao, C. M. Cahill, X. Huang, J. L. Roffman, S. Lamon-Fava, M. Fava, D. Mischoulon and J. T. Rogers, *Neurotherapeutics*, 2018, **15**, 156–175.
3 S. Hanna, L. Lachover and R. P. Rajarethinam, *Prim Care Companion J Clin Psychiatry*, 2009, **11**, 269–270.
4 M. H. Parvin, E. Azizi, J. Arjomandi and J. Y. Lee, *Sens. Actuators, B*, 2018, **261**, 335–344.
5 T. Koide, T. Ono, H. Shimakoshi and Y. Hisaeda, *Coord. Chem. Rev.*, 2022, **470**, 214690.
6 C. Tian, N. Zhao, X. Jiang, D. Wan and Y. Xie, *Water*, 2021, **13**, 1790.
7 H. R. Skeggs, H. M. Nepple, K. A. Valentik, J. W. Huff and L. D. Wright, *J. Biol. Chem.*, 1950, **184**, 211–221.
8 C. E. Hoffmann, E. L. R. Stokstad, B. L. Hutchings, A. C. Dornbush and T. H. Jukes, *J. Biol. Chem.*, 1949, **181**, 635–644.
9 E. Greibe and E. Nexo, *Clin. Chem. Lab. Med.*, 2011, **49**, 1883–1885.
10 D. Hampel, S. Shahab-Ferdows, J. M. Domek, T. Siddiqua, R. Raqib and L. H. Allen, *Food Chem.*, 2014, **153**, 60–65.
11 L. R. Snyder, J. W. Dolan and J. R. Gant, *J. Chromatogr.*, 1979, **165**, 3–30.
12 P. F. Chatzimichalakis, V. F. Samanidou, R. Verpoorte and I. N. Papadoyannis, *J. Sep. Sci.*, 2004, **27**, 1181–1188.
13 B. L. Karger, A. S. Cohen and A. Guttman, *J. Chromatogr. B: Biomed. Sci. Appl.*, 1989, **492**, 585–614.
14 G. B. J. Glass, L. J. Boyd, G. A. Gellin and L. Stephanson, *Arch. Biochem. Biophys.*, 1954, **51**, 251–257.
15 A. Doscherholmen, P. S. Hagen and M. Liu, *Blood*, 1957, **12**, 336–346.
16 S. Nie and R. N. Zare, *Annu. Rev. Biophys. Biomol. Struct.*, 1997, **26**, 567–596.
17 Z. Song and S. Hou, *Anal. Chim. Acta*, 2003, **488**, 71–79.
18 N. Akbay and E. Gök, *J. Anal. Chem.*, 2008, **63**, 1073–1077.
19 J. A. Murillo Pulgarín, L. F. García Bermejo and M. Nieves Sánchez García, *Luminescence*, 2011, **26**, 536–542.
20 H. Xu, Y. Li, C. Liu, Q. Wu, Y. Zhao, L. Lu and H. Tang, *Talanta*, 2008, **77**, 176–181.
21 J. Wang, J. Wei, S. Su and J. Qiu, *New J. Chem.*, 2015, **39**, 501–507.
22 J. Wang, H. Z. Zhang, R. S. Li and C. Z. Huang, *TrAC, Trends Anal. Chem.*, 2016, **80**, 429–443.
23 G. Tsiminis, E. P. Schartner, J. L. Brooks and M. R. Hutchinson, *Appl. Spectrosc. Rev.*, 2017, **52**, 439–455.
24 K. B. Akshaya, V. Anitha, M. Nidhin, Y. N. Sudhakar and G. Louis, *Talanta*, 2020, **217**, 121028.
25 M. Mylarappa, N. Raghavendra, B. S. Surendra, K. N. Shravana Kumar and S. Kantharjau, *Appl. Surf. Sci.*, 2022, **10**, 100268.
26 S. Shaktawat, K. R. Singh, S. Thapa, R. Verma, J. Singh and R. P. Singh, *Mater. Lett.: X*, 2023, **17**, 100187.
27 D. Thomele, S. O. Baumann, J. Schneider, A. K. Sternig, S. Shulda, R. M. Richards, T. Schwab, G. A. Zickler, G. R. Bourret and O. Diwald, *Cryst. Growth Des.*, 2021, **21**, 4674–4682.
28 A. Manuja, B. Kumar, R. Kumar, D. Chhabra, M. Ghosh, M. Manuja, B. Brar, Y. Pal, B. N. Tripathi and M. Prasad, *Toxicol. Rep.*, 2021, **8**, 1970–1978.
29 B. B. Pala, T. Vural, F. Kuralay, T. Çırak, G. Bolat, S. Abacı and E. B. Denkbaş, *Appl. Surf. Sci.*, 2014, **303**, 37–45.
30 M. Bhaiyya, P. K. Pattnaik and S. Goel, *Sens. Actuators, A*, 2021, **331**, 112831.
31 R. Rajeev, L. Benny, M. Roy, A. T. Mathew, K. B. Akshaya, A. Varghese and G. Hegde, *New J. Chem.*, 2022, **46**, 4114–4125.
32 Y. Li, M. Li, J. Rantanen, M. Yang and A. Bohr, *Int. J. Pharm.*, 2022, **611**, 121278.
33 C. S. Cundy and P. A. Cox, *Chem. Rev.*, 2003, **103**, 663–702.
34 P. E. J. Saloga, C. Kästner and A. F. Thünemann, *Langmuir*, 2018, **34**, 147–153.
35 C. B. Maliakkal, M. Tornberg, D. Jacobsson, S. Lehmann and K. A. Dick, *Nanoscale Adv.*, 2021, **3**, 5928–5940.
36 H. J. Imran, K. A. Hubeatir, K. A. Aadim and D. S. Abd, *J. Phys.: Conf. Ser.*, 2021, **1818**, 012127.
37 M. Parashar, V. K. Shukla and R. Singh, *J. Mater. Sci.: Mater. Electron.*, 2020, **31**, 3729–3749.
38 D. Li, S. He, J. Chen, C. Jiang and C. Yang, *IOP Conf. Ser.: Mater. Sci. Eng.*, 2017, **242**, 012023.
39 A. Almontasser, A. Parveen and A. Azam, *IOP Conf. Ser.: Mater. Sci. Eng.*, 2019, **577**, 012051.
40 V. Nariyal and P. Sharma, *Int. J. Adv. Res.*, 2017, **5**, 587–591.
41 S. Vijayakumar, M. Nilavukkarasi and P. K. Praseetha, *Vegetos*, 2021, **34**, 719–724.
42 S. A. Kumar, J. S. Shankar, B. K. Periyasamy and S. K. Nayak, *Phys. Chem. Chem. Phys.*, 2021, **23**, 22804–22816.
43 P. Malik, M. Srivastava, R. Verma, M. Kumar, D. Kumar and J. Singh, *Mater. Sci. Eng., C*, 2016, **58**, 432–441.

44 J. Jeevanandam, Y. S. Chan and M. K. Danquah, *New J. Chem.*, 2017, **41**, 2800–2814.
45 G. Balakrishnan, R. Velavan, K. Mujasam Batoo and E. H. Raslan, *Results Phys.*, 2020, **16**, 103013.
46 S. E.-D. Hassan, A. Fouda, E. Saied, M. M. S. Farag, A. M. Eid, M. G. Barghoth, M. A. Awad, M. F. Hamza and M. F. Awad, *J. Fungi*, 2021, **7**, 372.
47 L. Aghebati-Maleki, B. Salehi, R. Behfar, H. Saeidmanesh, F. Ahmadian, M. Sarebanhassanabadi and M. Negahdary, *Int. J. Electrochem. Sci.*, 2014, **9**, 257–271.
48 M. I. Khan, M. N. Akhtar, N. Ashraf, J. Najeeb, H. Munir, T. I. Awan, M. B. Tahir and M. R. Kabli, *Appl. Nanosci.*, 2020, **10**, 2351–2364.
49 R. Sreekanth, J. Pattar, A. V. Anupama and A. M. M. Mallikarjunaswamy, *Appl. Phys. A*, 2021, **127**, 797.
50 B. Nourozi, A. Aminian, N. Fili, Y. Zangeneh, A. Boochani and P. Darabi, *Results Phys.*, 2019, **12**, 2038–2043.
51 R. L. Nelson, J. W. Hale and B. J. Harmsworth, *Trans. Faraday Soc.*, 1971, **67**, 1164–1182.
52 L. Chen, C. Xu, X.-F. Zhang and T. Zhou, *Phys. E: Low-Dimens. Syst. Nanostructures.*, 2009, **41**, 852–855.
53 C. Boyadjian and L. Lefferts, *Catalysts*, 2020, **10**, 354.
54 S. Hussain, H. Chen, Z. Zhang and H. Zheng, *Chem. Commun.*, 2020, **56**, 2336–2339.
55 Z. Chen, Z. Wu, J. Sun, C. Mao and F. Su, *Tribol. Lett.*, 2021, **69**, 47.
56 J. Zhu, J. Sun, S. Tian, J. Yang, J. Feng and Y. Xiong, *Environ. Sci.: Nano*, 2020, **7**, 2723–2734.
57 P. Gao, X. Tian, C. Yang, Z. Zhou, Y. Li, Y. Wang and S. Komarneni, *Environ. Sci.: Nano*, 2016, **3**, 1416–1424.
58 S. Visweswaran, R. Venkatachalapathy, M. Haris and R. Murugesan, *J. Mater. Sci.: Mater. Electron.*, 2020, **31**, 14838–14850.
59 A. Almasian, F. Najafi, L. Maleknia and M. Giahi, *New J. Chem.*, 2018, **42**, 2013–2029.
60 A. H. Chowdhury, S. Ghosh and S. M. Islam, *New J. Chem.*, 2018, **42**, 14194–14202.
61 E. Laviron, *J. Electroanal. Chem. Interfacial Electrochem.*, 1979, **101**, 19–28.
62 R. Verma, K. R. Singh, R. Verma and J. Singh, *Luminescence*, 2023, **38**, 1393–1404.
63 M. M. Islam and R. Kant, *Electrochim. Acta*, 2011, **56**, 4467–4474.
64 P. Manivel, K. Madasamy, V. Suryanarayanan, N. Nesakumar, A. J. Kulandaisamy, M. Kathiresan, M. Parthiban, D. Velayutham and K. M. Lee, *J. Taiwan Inst. Chem. Eng.*, 2019, **96**, 1–10.
65 G. Dimitropoulou, S. Karastogianni and S. Girousi, *J. Appl. Bioanal.*, 2017, **3**, 70–80.